

## Full-Scale Sea Trials of a Motion Control System for ROVs Based on a High-Gain State Observer

Daniel de A. Fernandes\* Asgeir J. Sørensen\* Décio C. Donha\*\*

\* Centre for Autonomous Marine Operations and Systems (AMOS) – Dept. of  
Marine Technology – Norwegian Univ. of Science and Tech. (NTNU) –  
Trondheim, Norway (e-mail: daniel.fernandes@ntnu.no;  
dalmeidafernandes@gmail.com; asgeir.sorensen@ntnu.no)

\*\* University of São Paulo (USP) – São Paulo, Brazil – Dept. of Mechanical  
Engineering (e-mail: decdonha@usp.br)

---

**Abstract:** This paper reports selected results from full-scale sea trials, along with the description of the digital version implemented in practice, of a Motion Control System (MCS) previously proposed by the authors in the continuous-time domain, which has station keeping, i.e. dynamic positioning, and trajectory tracking capabilities for navigating observation class Remotely Operated Vehicles (ROV) used to carry out automated high-resolution image capturing missions, e.g. assessments, inspections, mappings, and surveys. Such capabilities are a key feature to enable the end-users of the ROV technology to acquire sequential high-quality images at proper pace to construct consistent representations of the objects or of the environments of interest. Four degrees-of-freedom are controlled, namely surge, sway, heave, and yaw. The MCS consists of an output feedback control system based on a high-gain state observer and a MIMO PID controller aided by reference feedforward. Feedback linearisation of the plant dynamics is also performed by the MCS. Satisfactory performance for suitable and sufficiently smooth reference trajectories are attained despite the presence of unmodelled dynamics, plant parameter variations, measurement noise, and environmental disturbances.

*Keywords:* Dynamic Positioning, Feedback Linearisation, High-Gain Observer, MIMO PID Control, Nonlinear Control, Output Feedback Control, ROV, Station Keeping, Trajectory Tracking.

---

### 1. INTRODUCTION

This paper reports selected results from full-scale sea trials, along with the description of the digital version implemented in practice, of the MCS proposed by Fernandes et al. (2013) navigating the NTNU's ROV Minerva in Trondheimsfjorden, Norway, in 2013. The MCS was initially studied in the continuous-time domain in Fernandes et al. (2013), where promising results based on computer simulations were presented; however, experimental results to validate those simulation results were missing. The present work thus aims at extending that performance appraisal. The performance of a High-Gain State Observer (HGSO) used to reconstruct and filter the measurements fed into the MCS is the main focus here.

The MCS has station keeping, i.e. Dynamic Positioning (DP), and trajectory tracking capabilities to navigate observation class ROVs. This type of ROV is used worldwide as an important carrier of imagery devices, e.g. cameras, sonars, echo sounders, and hyperspectral imagers, for industrial, military, and research activities, e.g. assessments, inspections, mappings, and surveys (Marsh et al., 2013; Christ and Wernli, 2007; Ludvigsen et al., 2007; Singh et al., 2007). The output feedback MCS shown in Fig. 1 essentially consists of the HGSO and a MIMO PID controller aided by reference feedforward. Feedback linearisation of the plant dynamics is implemented in the MCS. Suitable and sufficiently smooth reference trajectories are generated by the guidance subsystem of the MCS based on the reference model proposed by Fernandes et al. (2012), which synthesises class  $C^2$ ,  $C^1$ , and  $C^0$ , position, velocity, and acceleration references,

respectively, to parameterise the reference trajectories. Reference models are usually employed in reference tracking control systems to improve their closed-loop transient responses; system constraints and input limits (bandwidths and amplitudes) are concerned, thereby avoiding performance deterioration and instability, in more severe cases (Åström and Hägglund, 2011; Franklin et al., 2009; Khalil, 2002). The guidance subsystem is not further detailed in this paper. The locally inertial North-East-Down (NED) coordinate frame (Fossen, 2011) is used for locally flat Earth navigation.

The HGSO has the ability to robustly estimate the unmeasured plant states, while asymptotically attenuating disturbances. It behaves approximately like a differentiator, hence fitting well applications where velocities may not be directly measured, but reconstructed from noisy position and/or attitude measurements (Khalil, 2002; Atassi and Khalil, 2000; Esfandiari and Khalil, 1992). A HGSO is tried out for the MCS as an alternative to the benchmark Extended Kalman Filter (EKF), which is an extension into nonlinear systems of the celebrated optimal linear-quadratic estimator Kalman filter (Fossen, 2011; Friedland, 1986). Despite the outstanding merit of the EKF, tuning it may be a hard and time-consuming task due to its quite numerous covariance parameters. Also, it often needs more memory space to be stored in a digital system, and runs slower, than alternative asymptotic state estimation techniques. An EKF is successfully used for motion control of ROVs in Sørensen et al. (2012). Other alternatives to the EKF, e.g. integrator backstepping and passivity, can be found in Fossen (2011), for instance.

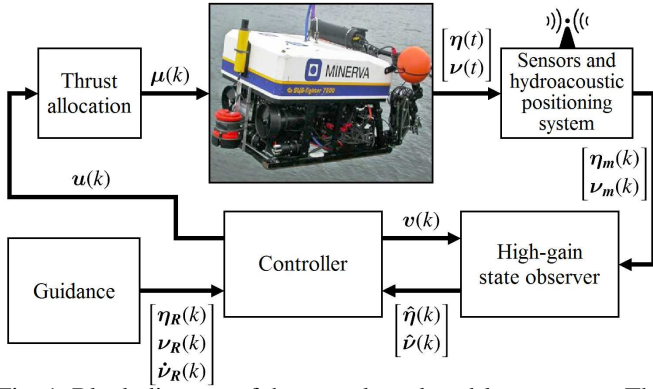


Fig. 1. Block diagram of the complete closed-loop system. The ROV (illustrated by Minerva) is the only subsystem evolving in the continuous-time domain, whereas all the other blocks compose the MCS and evolve in the discrete-time domain. The variables are introduced in Sections 2 and 3.

The classical PID controller is often preferred for motion control of ROVs, and likewise for industrial applications in general (Åström and Hägglund, 2011; Smallwood and Whitcomb, 2004; Hsu et al., 2000), despite the availability of several modern and advanced control techniques. Although it has limitations to cope with highly coupled multivariable plants, it is often preferred due to its synthesis and implementation simplicity (Åström and Hägglund, 2011; Franklin et al., 2009; Friedland, 1986). It cannot provide exact tracking of time-varying references alone, neither can it dynamically compensate for unmodelled plant dynamics; nonetheless, such limitations can be circumvented by combining other techniques with the PID algorithm. A number of successful PID-based marine applications can be found in the literature, e.g. Omerdic et al. (2012), Sørensen et al. (2012), and Smallwood and Whitcomb (2004).

Position and heading angle measurements at least are required by the MCS. The (digital) navigation sensors feed data into the MCS at different rates. The horizontal position measurements, usually generated by hydroacoustic positioning systems based on either the (Super) Short Base Line or Long Base Line principle (Christ and Wernli, 2007), have (much) lower update rates ( $< 1$  Hz) than the sampling frequency of the MCS, imposing the major limitations to the overall motion control accuracy. The pressure gauge and gyrocompass providing the MCS with depth and heading angle measurements, respectively, present fairly high update rates. The MCS may also be provided with velocity measurements for enhanced motion control accuracy. Such measurements, typically coming from Doppler Velocity Logs (DVL) (Christ and Wernli, 2007), are also generated at lower update rates ( $\cong 1$  Hz) than the sampling frequency of the MCS.

The paper is organised as follows. Section 2 reviews the plant model. Section 3 presents the MCS. Section 4 presents results from full-scale sea trials. Section 5 presents concluding remarks. Appendix A introduces the NTNU's ROV Minerva.

## 2. CONTROL PLANT MODEL

The proposed Control Plant Model (CPM) (Sørensen, 2013) follows the formulations and nomenclature defined by SNAME (1950). It is based on the models found in Sørensen (2013), Fossen (2011), and Lewandowski (2004). Its explicit dependence on the time  $t$  is omitted for the sake of simplicity. It is built on the following premisses: (i) the ROV is fully actuated in the configuration space (Breivik and Fossen, 2009), i.e. the four

controlled Degrees-of-Freedom (DoF) are actuated; (ii) the remaining two DoFs are self-stable by the design of the ROV; (iii) the Centre of Gravity (CG) and the Centre of Buoyancy (CB) are both fixed; (iv) the ROV operates below the wave-affected zone; (v) the velocity and orientation of the sea current vary very slowly enough to be taken as constant; and (vi) the fluid is irrotational, of constant density, and of infinite extent.

The CPM is given by

$$\begin{cases} \dot{\eta} = J(\psi) \nu \\ M \dot{\nu} = -C(\nu) \nu - D_L \nu - D_Q |\nu| \nu + g + c + \tau \end{cases} \quad (1)$$

where  $J(\psi) \in SO(4)$  (Special Orthogonal group of order 4) is a transformation matrix from the BF (Body-Fixed) coordinate frame to the NED frame, and  $\nu = [u, v, w, r]^T$  is the relative velocity vector given in the BF frame. The vector of signed squares  $|\nu| \nu := [|u|u, |v|v, |w|w, |r|r]^T$  represents quadratic relative velocities. The position and heading angle vector  $\eta = [n, e, d, \psi]^T$  gives the position from the chosen origin of the NED frame, and the heading angle with respect to the N-axis of the NED frame. The inertia matrix  $M \in \mathbb{R}^{4 \times 4} \mid M := M_{RB} + M_A > 0$  embodies the mass and the inertia tensor of the rigid-body ( $M_{RB} \in \mathbb{R}^{4 \times 4} \mid M_{RB} > 0$ ), and the hydrodynamic added masses and the corresponding inertia tensor ( $M_A \in \mathbb{R}^{4 \times 4} \mid M_A \geq 0$ ). The Coriolis-centripetal matrix  $C(\nu) := C_{RB}(\nu) + C_A(\nu) \in SS(4)$  (Skew-Symmetric group of order 4) is directly derived from  $M$ . The matrix  $D_L \in \mathbb{R}^{4 \times 4} \mid D_L > 0$  collects linear hydrodynamic damping coefficients regarding linear skin friction (laminar flow). The matrix  $D_Q \in \mathbb{R}^{4 \times 4} \mid D_Q > 0$  collects quadratic hydrodynamic damping coefficients regarding quadratic skin friction and vortex shedding (turbulent flow). All elements of  $M$ ,  $D_L$ , and  $D_Q$  are expected to be nonzero and distinct, as the ROV has an open-frame structure with asymmetries in the shapes and distribution of its internal parts and components. Besides, every element of these matrices may split into a pair of relatively close values regarding positive and negative velocities for each DoF, and may yet vary about the nominal values (Lewandowski, 2004; Caccia et al., 2000). The vector of hydrostatic restoring forces  $g = [0, 0, (W - B), 0]^T$  collects the weight force  $W = mg$  acting upon the CG, and the buoyancy force  $B = \rho \nabla g$  acting upon the CB, where  $m$  is the ROV's (dry) mass,  $g$  is the acceleration of gravity,  $\rho$  is the fluid density, and  $\nabla$  is the total volume of fluid displaced by the ROV. A safer design ensures that the ROV is slightly positive buoyant, i.e.  $B > W$ , whereupon the ROV is able to emerge to the surface without the aid of the MCS, if necessary. The vector  $c \in \mathbb{R}^4$  represents unmeasured (nonestimated either) current-generated perturbing forces and moment, as the speed and direction of the sea current are neither measured nor estimated in this work. Notice that (1) is based only on body-fixed velocities. The vector  $\tau \in \mathbb{R}^4 \mid \tau := T_P [T_1, T_2, \dots, T_p]^T$  represents the propulsion and steering forces and moment delivered by the propulsion system, where  $T_i := k_{T_i}(\omega_i) |\omega_i| \omega_i$ ,  $i \in \mathbb{N} \mid i = \{1, \dots, p\}$ , is the thrust delivered by the  $i$ -th thruster, under the common simplifying assumption that the static mappings  $k_{T_i}(\omega_i)$ , which also encompass all the losses, hold from the revolution rates of the propeller discs  $\omega_i$  to the developed thrusts  $T_i$  (Sørensen et al., 2012; Fossen, 2011; Caccia et al., 2000),  $T_P \in \mathbb{R}^{4 \times p}$  is the thrust configuration matrix of the propulsion system, and  $p \geq 4$  is the number of thrusters which actuate the configuration space (Breivik and Fossen, 2009). The matrix  $T_P$  is typically constant because the ROV typically has thrusters with fixed pitch propellers installed at fixed locations.

### 3. MOTION CONTROL SYSTEM

#### 3.1 Introduction

The MCS runs synchronously at the constant sampling frequency  $f_s$ . This implies that the vector  $\boldsymbol{\mu}(\cdot)$  controlling the thrusters through zero-order-hold circuits (Franklin et al., 2009; Åström and Wittenmark, 1997) located in the thrust allocation block, i.e. interfacing the MCS and the plant, see Fig. 1, is updated at every sampling instant, and also that the HGSO simultaneously takes the most recent navigation data stored in a data buffer created in the MCS to serve this purpose. The updates of  $\boldsymbol{\mu}(\cdot)$  are then computed in between two consecutive sampling instants based on the most recently taken data from the buffer. The different navigation sensors and the hydroacoustic positioning system feed data into the data buffer asynchronously. The sensors having update rates higher than  $f_s$  renew the corresponding portion of the data buffer several times per sampling period  $h := f_s^{-1}$ . The sensors having update rates (much) lower than  $f_s$  cause the same data stored in the corresponding portion of the data buffer to be reused for multiple sampling periods.

#### 3.2 Controller

The controller subsystem, see Fig. 1, essentially consists of a MIMO PID controller aided by reference feedforward. It also includes feedback linearisation of the plant dynamics. The control vector  $\boldsymbol{v}(\cdot) \in \mathbb{R}^4$  controls the HGSO. The control vector  $\boldsymbol{u}(\cdot) \in \mathbb{R}^4$  controls the plant through the thrust allocation block.

The control vectors  $\boldsymbol{v}(\cdot)$  and  $\boldsymbol{u}(\cdot)$  are defined as

$$\begin{cases} \boldsymbol{v}(k) := \boldsymbol{u}_{PID}(k-1) + \boldsymbol{u}_{FF}(k) \\ \boldsymbol{u}(k) := \boldsymbol{v}(k) + \boldsymbol{u}_{LIN}(k) \end{cases} \quad (2)$$

where  $k \in \mathbb{N} | k \geq 1$ ,  $\boldsymbol{u}_{PID}(\cdot)$  implements full state feedback,  $\boldsymbol{u}_{FF}(\cdot)$  provides reference feedforward, and  $\boldsymbol{u}_{LIN}(\cdot)$  tackles to cancel out the nonlinearities in the dynamics of (1). The term  $\boldsymbol{u}_{PID}(\cdot)$  is taken one sampling period delayed to preclude the algebraic loop between the MIMO PID controller and the HGSO, as they feed each other. All terms are detailed in the sequence.

The feedback linearisation term  $\boldsymbol{u}_{LIN}(\cdot)$  is defined as

$$\boldsymbol{u}_{LIN}(k) := \overline{\boldsymbol{C}}(\hat{\boldsymbol{v}}(k))\hat{\boldsymbol{v}}(k) + \overline{\boldsymbol{D}_Q}|\hat{\boldsymbol{v}}(k)|\hat{\boldsymbol{v}}(k) - \overline{\boldsymbol{g}} \quad (3)$$

where  $\overline{\boldsymbol{C}}(\hat{\boldsymbol{v}}(\cdot)), \overline{\boldsymbol{D}_Q} \in \mathbb{R}^{4 \times 4}$ , and  $\overline{\boldsymbol{g}} \in \mathbb{R}^4$  are the nominal expressions of  $\boldsymbol{C}(\boldsymbol{v})$ ,  $\boldsymbol{D}_Q$ , and  $\boldsymbol{g}$ , and  $\hat{\boldsymbol{v}}(\cdot) \in \mathbb{R}^4$  is the vector of estimated velocities. It is properly introduced in Subsection 3.3.

The state feedback term  $\boldsymbol{u}_{PID}(\cdot)$  is defined as

$$\boldsymbol{u}_{PID}(k) := \boldsymbol{K}_P \boldsymbol{e}_\eta(k) + \boldsymbol{K}_I \boldsymbol{e}_I(k) + \boldsymbol{K}_D \boldsymbol{e}_v(k) \quad (4)$$

where  $\boldsymbol{K}_P, \boldsymbol{K}_I, \boldsymbol{K}_D \in \mathbb{R}^{4 \times 4} | \boldsymbol{K}_P, \boldsymbol{K}_I, \boldsymbol{K}_D > 0$  are (typically diagonal) matrices holding the proportional, integral, and derivative gain sets of the MIMO PID controller, and the error vectors  $\boldsymbol{e}_\eta(\cdot), \boldsymbol{e}_I(\cdot), \boldsymbol{e}_v(\cdot) \in \mathbb{R}^4$  are defined as

$$\begin{cases} \boldsymbol{e}_\eta(k) := \boldsymbol{J}^T(\hat{\psi}(k-1))(\boldsymbol{\eta}_R(k) - \hat{\boldsymbol{\eta}}(k)) \\ \boldsymbol{e}_I(k) := \boldsymbol{e}_I(k-1) + (h/2)(\boldsymbol{e}_\eta(k) + \boldsymbol{e}_\eta(k-1)) \\ \boldsymbol{e}_v(k) := \boldsymbol{\nu}_R(k) - \hat{\boldsymbol{v}}(k) \end{cases} \quad (5)$$

where  $\hat{\psi}(\cdot)$  is the estimated heading angle used everywhere in the MCS to keep the coordinate transformations synchronised,

$\hat{\boldsymbol{\eta}}(\cdot) \in \mathbb{R}^4$  is the vector of estimated position and heading angle whose last component is  $\hat{\psi}(\cdot)$ ,  $\boldsymbol{\eta}_R(\cdot) \in \mathbb{R}^4$  is the vector of reference position and heading angle whose last component is the reference heading angle  $\psi_R(\cdot)$ ,  $\boldsymbol{\nu}_R(\cdot) \in \mathbb{R}^4$  is the vector of reference velocities, such that  $\boldsymbol{\nu}_R(t) := \boldsymbol{J}^T(\psi_R(t)) \frac{d}{dt}[\boldsymbol{\eta}_R(t)]$ . This continuous-time representation is used for the sake of simplicity. The vector  $\hat{\boldsymbol{\eta}}(\cdot)$  is properly introduced in Subsection 3.3.

The bilinear Tustin's approximation method is used for numerical integration in (5), as it maps the whole left-hand  $s$ -plane into the unit circle in the  $z$ -plane, hence always yielding stable discrete-time approximations from originally stable continuous-time systems. Also, it typically provides pretty close response approximations between the continuous- and discrete-time domains (Franklin et al., 2009; Åström and Wittenmark, 1997). A numerical differentiator is advantageously unnecessary in (5), as the error vector  $\boldsymbol{e}_v(\cdot)$  is directly available. Numerical differentiation algorithms can be quite sensitive to noise.

*Remark:* Other functionalities, e.g. reset and anti-windup, can also be added to the basic integrator algorithm in (5) to enhance the integration performance and make it more robust.

The reference feedforward term  $\boldsymbol{u}_{FF}(\cdot)$  is defined as

$$\boldsymbol{u}_{FF}(k) := \overline{\boldsymbol{D}_L} \boldsymbol{\nu}_R(k) + \overline{\boldsymbol{M}} \dot{\boldsymbol{\nu}}_R(k) \quad (6)$$

where  $\overline{\boldsymbol{D}_L}, \overline{\boldsymbol{M}} \in \mathbb{R}^{4 \times 4}$  are the nominal expressions of  $\boldsymbol{D}_L$  and  $\boldsymbol{M}$ , and  $\dot{\boldsymbol{\nu}}_R(\cdot) \in \mathbb{R}^4$  is the vector of reference accelerations, where  $\dot{\boldsymbol{\nu}}_R(t) := \frac{d}{dt}[\boldsymbol{\nu}_R(t)]$ . This continuous-time representation is employed here only for the sake of simplicity.

Proper initialisation of the vectors is an important precaution in order to avoid unpredictable initial behaviour. It is suggested that  $\boldsymbol{e}_\eta(0) = \boldsymbol{e}_I(0) = \boldsymbol{u}_{PID}(0) = \boldsymbol{v}(0) = \mathbf{0}$ ,  $\boldsymbol{\eta}_R(1) = \hat{\boldsymbol{\eta}}(1)$ ,  $\boldsymbol{\nu}_R(1) = \hat{\boldsymbol{v}}(1)$ , and  $\dot{\boldsymbol{\nu}}_R(1) = \mathbf{0}$ . The initialisation of  $\hat{\boldsymbol{v}}(\cdot)$  and  $\hat{\boldsymbol{\eta}}(\cdot)$  is discussed within Subsection 3.3.

The thrust allocation block converts the vector  $\boldsymbol{u}(\cdot)$  into  $p$  individual signals  $\boldsymbol{\mu}_i(\cdot)$  (either voltages or currents) controlling the thruster servos, where  $\boldsymbol{\mu}(\cdot) \in \mathbb{R}^p | \boldsymbol{\mu}(\cdot) := [\boldsymbol{\mu}_1(\cdot), \boldsymbol{\mu}_2(\cdot), \dots, \boldsymbol{\mu}_p(\cdot)]^T$ . Therefore, these signals ultimately produce the vector  $\boldsymbol{\tau}$  in (1). They are computed as  $\boldsymbol{\mu}_i(\cdot) := \theta_i \operatorname{sgn}(T_i) \sqrt{|T_i|/k_{T_i}(\omega_i)}$ ,  $i = \{1, \dots, p\}$ , where  $T_i$  and  $k_{T_i}(\omega_i)$  are described in Section 2,  $\theta_i \in \mathbb{R}_{>0} | \theta_i := \boldsymbol{\mu}_i(\cdot)/\omega_i$  are scaling factors (inverse servo gains) relating the signals  $\boldsymbol{\mu}_i(\cdot)$  to the propeller angular velocities  $\omega_i$ , and  $[T_1, T_2, \dots, T_p]^T := \boldsymbol{T}_P^* \boldsymbol{u}$ . The thrust allocation algorithm consists of the mapping  $\boldsymbol{T}_P^* := \boldsymbol{W}_P^{-1} \boldsymbol{T}_P^T (\boldsymbol{T}_P \boldsymbol{W}_P^{-1} \boldsymbol{T}_P^T)^{-1}$ , which is essentially the Moore-Penrose pseudo-inverse of the thrust configuration matrix  $\boldsymbol{T}_P$  described in Section 2. The (typically diagonal) matrix  $\boldsymbol{W}_P \in \mathbb{R}^{p \times p} | \boldsymbol{W}_P = \boldsymbol{W}_P^T > 0$  weights the thrust usage, so that it is possible to reach an optimal thrust allocation through the minimisation of the quadratic cost function  $J := \min([T_1, \dots, T_p] \boldsymbol{W}_P [T_1, \dots, T_p]^T)$  subject to  $\boldsymbol{\tau} = \boldsymbol{T}_P [T_1, \dots, T_p]^T$ .

#### 3.3 High-gain state observer

The vector of estimated states  $[\hat{\boldsymbol{\eta}}^T(\cdot), \hat{\boldsymbol{v}}^T(\cdot)]^T \in \mathbb{R}^8$  is given by

$$\begin{bmatrix} \hat{\boldsymbol{\eta}}(k) \\ \hat{\boldsymbol{v}}(k) \end{bmatrix} = \boldsymbol{\Phi}(\hat{\psi}(k-1)) \begin{bmatrix} \hat{\boldsymbol{\eta}}(k-1) \\ \hat{\boldsymbol{v}}(k-1) \end{bmatrix} + \boldsymbol{\Gamma}_V(\hat{\psi}(k-1))(\boldsymbol{v}(k) + \boldsymbol{v}(k-1)) \\ + \boldsymbol{\Gamma}_Y(\hat{\psi}(k-1)) \left( \begin{bmatrix} \hat{\boldsymbol{\eta}}_m(k) \\ \boldsymbol{\nu}_m(k) \end{bmatrix} + \begin{bmatrix} \hat{\boldsymbol{\eta}}_m(k-1) \\ \boldsymbol{\nu}_m(k-1) \end{bmatrix} \right) \quad (7)$$

where  $v(\cdot)$  is defined in (2),  $\nu_m(\cdot) \in \mathbb{R}^4$  is the vector of measured velocities, and  $\bar{\eta}_m(\cdot) \in \mathbb{R}^4$  is the vector of measured position and accumulated heading angle obtained partially directly from the vector of measured position and heading angle  $\eta_m(\cdot) \in \mathbb{R}^4$  and partially through a heading angle accumulation algorithm enabling the MCS to keep track of the number of turns the ROV performs. The algorithm and the vector  $\bar{\eta}_m(\cdot)$  are further described ahead. The vector  $\nu_m(\cdot) = \mathbf{0} \forall k \in \mathbb{N}$  whenever velocities are not measured. The system matrix  $\Phi(\hat{\psi}(\cdot)) \in \mathbb{R}^{8 \times 8}$ , the control input matrix  $\Gamma_V(\hat{\psi}(\cdot)) \in \mathbb{R}^{8 \times 4}$ , and the output injection matrix  $\Gamma_Y(\hat{\psi}(\cdot)) \in \mathbb{R}^{8 \times 8}$  are defined as

$$\Phi(\hat{\psi}(k-1)) := \Delta(\hat{\psi}(k-1)) (\mathbf{I}_8 + \Lambda(\hat{\psi}(k-1))) \quad (8)$$

$$\Gamma_V(\hat{\psi}(k-1)) := \Delta(\hat{\psi}(k-1)) \begin{bmatrix} \mathbf{0}_4 \\ (h/2) \bar{M}^{-1} \end{bmatrix} \quad (9)$$

$$\Gamma_Y(\hat{\psi}(k-1)) := \Delta(\hat{\psi}(k-1)) T(\hat{\psi}(k-1)) \frac{h}{2} L T^T(\hat{\psi}(k-1)) \quad (10)$$

where  $T(\hat{\psi}(\cdot)) := \text{blockdiag}(J(\hat{\psi}(\cdot)), \mathbf{I}_4) \in SO(8)$  (Special Orthogonal group of order 8) is a transformation matrix, where  $\mathbf{I}_i \in \mathbb{R}^{i \times i}$ ,  $i \in \{4, 8\}$ , are identity matrices,  $\mathbf{0}_4 \in \mathbb{R}^{4 \times 4}$  is a zero matrix, and the matrices  $\Delta(\hat{\psi}(\cdot)), \Lambda(\hat{\psi}(\cdot)) \in \mathbb{R}^{8 \times 8}$  are defined as

$$\Delta(\hat{\psi}(k-1)) := (\mathbf{I}_8 - \Lambda(\hat{\psi}(k-1)))^{-1} \quad (11)$$

$$\Lambda(\hat{\psi}(k-1)) := T(\hat{\psi}(k-1)) \frac{h}{2} (\mathbf{A} - \mathbf{L}) T^T(\hat{\psi}(k-1)) \quad (12)$$

where

$$\mathbf{A} := \begin{bmatrix} \mathbf{0}_4 & \mathbf{I}_4 \\ \mathbf{0}_4 & -\bar{M}^{-1} \bar{D}_L \end{bmatrix} \quad \text{and} \quad \mathbf{L} := \begin{bmatrix} \epsilon^{-1} L_{11} & \gamma \epsilon^{-1} L_{12} \\ \epsilon^{-2} L_{21} & \gamma \epsilon^{-2} L_{22} \end{bmatrix} \quad (13)$$

where  $L_{ij} \in \mathbb{R}^{4 \times 4}$ ,  $i, j = \{1, 2\}$ , are constant tuning submatrices, the constant  $\epsilon \in \mathbb{R}_{>0} \mid \epsilon \ll 1$  is a global tuning parameter yielding the high gains, and the constant  $\gamma \in \mathbb{N} \mid \gamma \in \{0, 1\}$ , where  $\gamma = 1$  indicates that velocities are measured.

The bilinear Tustin's approximation method is used for numerical integration in (7), for the same previously stated reasons. Notice that  $\hat{\psi}(k-1)$ , which is used to perform synchronised coordinate transformations throughout the MCS, is taken one sampling period delayed to preclude an algebraic loop in the HGSO, since the HGSO also feeds  $\hat{\psi}(\cdot)$  into itself. Notice also that  $\eta_m(\cdot)$ ,  $\bar{\eta}_m(\cdot)$ , and  $\nu_m(\cdot)$  are manipulated, i.e. read and written, by the HGSO, whereas the data buffer described in Subsection 3.1 is only read by the HGSO.

The heading angle measurement  $\psi_m(\cdot)$ , which is the last element of  $\eta_m(\cdot)$ , is typically commercially obtainable in the ranges: (i)  $\psi_m(\cdot) \in [0, 2\pi)$ ; and (ii)  $\psi_m(\cdot) \in (-\pi, \pi]$ . In either case the range is discontinuous and limited, so that the heading angle is not accumulated along consecutive turns. The simplest occurrence example happens when a turn is completed regarding the range (i). The Algorithm 1 can then be used to overcome this condition, for instance, where  $counter(\cdot) \in \mathbb{Z}$  is to be initialised as  $counter(0) = counter(1) = 0$ , and  $range \in \mathbb{N} \mid range \in \{1, 2\}$ , where  $range = 1$  corresponds to the range (i), and  $range = 2$  corresponds to the range (ii). Finally, the three position measurements in  $\eta_m(\cdot)$ , i.e. its three first elements, are just copied into  $\bar{\eta}_m(\cdot)$  and the accumulated heading angle  $\psi_{acc}(\cdot)$  coming out from Algorithm 1 completes  $\bar{\eta}_m(\cdot)$ .

---

```

if range = 2  $\wedge$   $\psi_m(k) < 0$  then
  |  $\psi_m(k) \leftarrow 2\pi + \psi_m(k)$ 
end
if range = 2  $\wedge$   $\psi_m(k-1) < 0$  then
  |  $\psi_m(k-1) \leftarrow 2\pi + \psi_m(k-1)$ 
end
if  $|\psi_m(k) - \psi_m(k-1)| \geq \pi$  then
  | if  $\psi_m(k-1) > \psi_m(k)$  then
  | | counter(k)  $\leftarrow$  counter(k-1) + 1
  | else
  | | counter(k)  $\leftarrow$  counter(k-1) - 1
  | end
end
 $\psi_{acc}(k) \leftarrow 2\pi counter(k) + \psi_m(k)$ 

```

---

**Algorithm 1.** Heading angle accumulation

It is suggested for proper initialisation of the HGSO that the estimation vectors agree with the measurement vectors, i.e.  $\hat{\eta}(0) = \hat{\eta}(1) = \bar{\eta}_m(0) = \bar{\eta}_m(1)$  and  $\hat{\nu}(0) = \hat{\nu}(1) = \nu_m(0) = \nu_m(1)$ , in order to zero the initial estimation errors. The ROV must preferably be at rest during the initialisation procedure, so that it is reasonable to assume that  $\hat{\nu}(1) = \nu_m(1) = \mathbf{0}$ . This action is essential to preclude, or at least to drastically attenuate, the characteristic initial high-valued short-duration peaks occurring in the vector  $[\hat{\eta}^T(\cdot), \hat{\nu}^T(\cdot)]^T$  (peaking phenomenon).

#### 4. RESULTS FROM FULL-SCALE SEA TRIALS

The sampling period  $h = 150$  ms was held during all trials.

The first step performed was tuning the HGSO for the condition without velocity measurements. The values reported in Fernandes et al. (2013), i.e.  $L_{11} = L_{21} = \bar{M}^{-1}$  and  $L_{12} = L_{22} = \mathbf{0}_4$ , were initially tried, followed by fine-tuning. After some interactions, it was realised that the option yielding the best results was  $L_{11} = L_{21} = 2\bar{M}^{-1}$ . Different values were also interactively assigned to  $\epsilon$ , and the value  $\epsilon = 0.1$  turned out eventually to be the best. These values indicate a reasonable adherence between the real and the modelled closed-loop systems.

It was confirmed during the tuning exercise that the output injection matrix  $\mathbf{L}$  in (13) damps the observed response in such a manner that a trade-off is established between relying more upon the response that is predicted based on the CPM, or relying more upon the incoming measurements instead. The greater the amount of damping represented by greater submatrices  $L_{ij}$ , the slower the estimation response with regard to changes in the measurements. On the other hand, the lesser  $\epsilon$ , the higher the magnitude of the eigenvalues of  $\mathbf{L}$ , whereupon the faster the estimation response. This happens because the reaction velocity (sensitivity) to fast changes in the measurements is proportional to the magnitude of such eigenvalues, and so is the sensitivity to measurement noise. Nevertheless, studying this problem in the framework of marine control systems is very interesting, because the controlled plants typically have (very) slow and overdamped dynamics. Therefore, a HGSO can be satisfactorily tuned, being assigned gains relatively much higher than those of the closed-loop systems formed by the controllers and the controlled plants, without actually holding too high gains in absolute terms. The peaking phenomenon is concomitantly attenuated if the gains of the HGSO are not too high.

Fig. 2–4 depict results from a station keeping trial (DP), where the heading angle was changed twice  $\pm\pi/2$  rad ( $\pm 90^\circ$ ). Velocity measurements were not used by the HGSO, in spite of

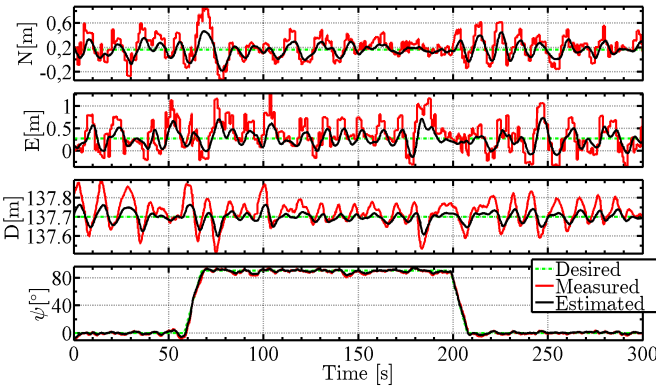


Fig. 2. DP trial: Position and heading angle.

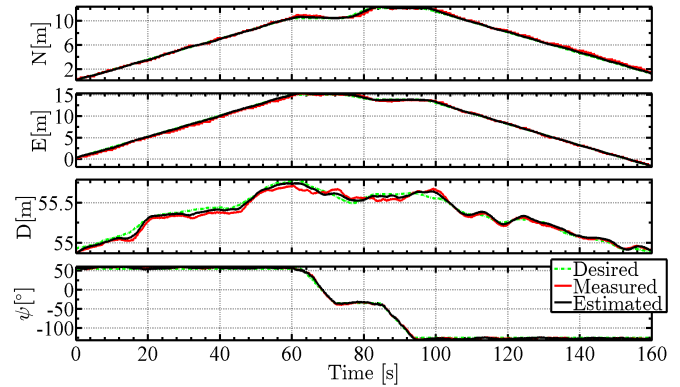


Fig. 5. Tracking trial: Position and heading angle.

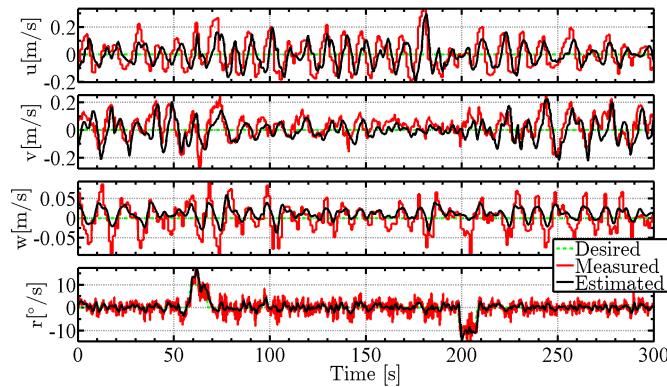


Fig. 3. DP trial: Velocities.

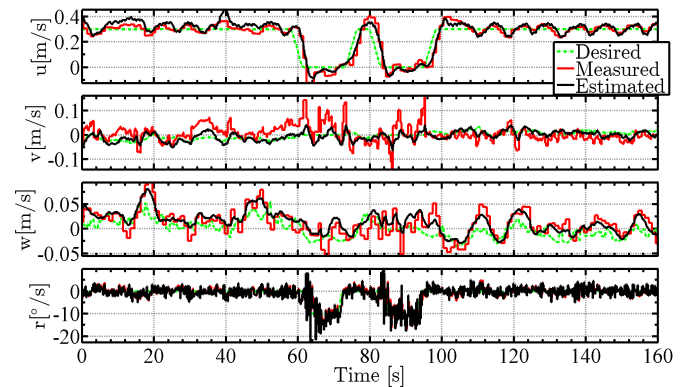


Fig. 6. Tracking trial: Velocities.

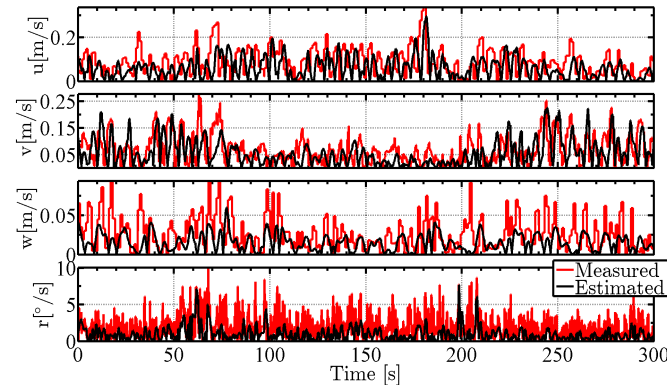


Fig. 4. DP trial: Absolute velocity errors w.r.t. references.

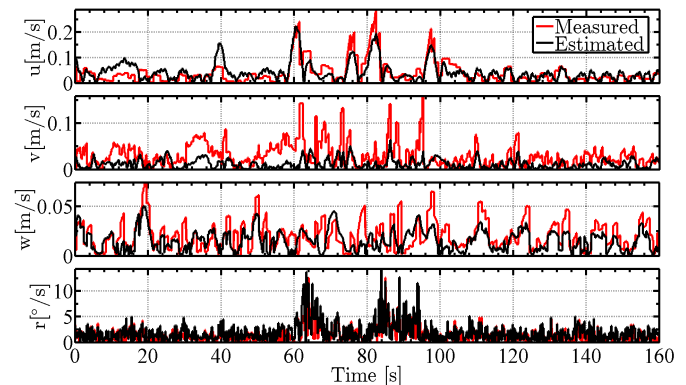


Fig. 7. Tracking trial: Absolute velocity errors w.r.t. references.

being available for comparison purposes. Fig. 2 shows stable and fairly satisfactory performance. The position measurements were reasonably well filtered, even without the support of additional velocity measurements. It is clear that the depth and the heading angle were more effectively kept closer to the desired set-points, due to their inherently favourable measurement characteristics, i.e. high update rates, yielding small differences between consecutive measurements. Fig. 3–4 show fairly good velocity reconstruction, in particular of the heave and yaw DoFs, reconfirming that better results can be attained under more reliable measurements. It is important to consider that part of the delay observed between the reconstructed and the measured velocities is caused by the differences between the hydroacoustic positioning system and the DVL.

Later, the HGSO was tuned for the condition with velocity measurements. After some interactions, the values  $L_{11} = L_{21} = 2 \bar{M}^{-1}$ ,  $L_{21} = L_{22} = 5 \bar{M}^{-1}$ , and  $\epsilon = 0.1$  were adopted. The tuning of the MIMO PID controller was held the same as

before. It was verified that the sensitivity to measurement noise, in particular, due to the unfavourable inherent characteristics of the horizontal position measurements, diminished considerably.

Fig. 5–7 depict results from a lawn-mower pattern tracking trial with simultaneous bottom profile tracking at constant altitude comprising two parallel legs of 20 m separated by a distance of 2 m. Velocity measurements were used by the HGSO this time. Fig. 5 shows that the MCS performed stably and satisfactorily in response to the suitable and sufficiently smooth references generated by the guidance subsystem. The position measurements were filtered better than in the previous DP trial. Fig. 6–7 show that the velocities were also well filtered. The maximum absolute position error was less than 20 cm, whereas the maximum absolute heading error was less than  $0.0873$  rad ( $5^\circ$ ). This is indeed a satisfactory result attained by the MCS. In practice, such result would enable the end-users of the ROV technology to acquire sequential high-quality images to construct representations of objects or environments of interest.

## 5. CONCLUDING REMARKS

The proposed output feedback MCS based on a HGSO was successfully tested in practice. It attained stable and satisfactory station keeping and trajectory tracking performances under challenging operating conditions, i.e. unmodelled dynamics, plant parameter variations, measurement noise, and environmental disturbances, validating the previously presented simulation results. In particular, the results presented in this paper encourage further research towards using the HGSO to replace the benchmark EKF. Further work is still needed in order to achieve harmonious tuning between the MIMO PID controller and the HGSO.

## ACKNOWLEDGEMENTS

The present work is part of the work carried out at AMOS and at the Applied Underwater Robotics Laboratory (AUR-Lab). It is supported by the Research Council of Norway through the Centres of Excellence funding scheme under the project No. 223254 – AMOS, and the project No. 192427.

## REFERENCES

- Åström, K.J. and Hägglund, T. (2011). *PID controllers: theory, design, and tuning*. Instrument Society of America, North Carolina, 2nd edition.
- Åström, K.J. and Wittenmark, B. (1997). *Computer-controlled systems: theory and design*. Prentice Hall, Inc., Upper Saddle River, 2nd edition.
- Atassi, A.N. and Khalil, H.K. (2000). Separation results for the stabilization of nonlinear systems using different high-gain observer designs. *International Journal of Control*, 39(3), 183–191.
- Breivik, M. and Fossen, T.I. (2009). Guidance laws for autonomous underwater vehicles. In A.V. Inzartsev (ed.), *Underwater Vehicles*, chapter 4, 51–76. I-Tech, Vienna, Austria.
- Caccia, M., Indiveri, G., and Veruggio, G. (2000). Modeling and identification of open-frame variable configuration unmanned underwater vehicles. *Journal of Oceanic Engineering*, 25(2), 227–240.
- Christ, R.D. and Wernli, R.L. (2007). *The ROV manual: a user guide for observation class remotely operated vehicles*. Butterworth-Heinemann, Oxford, UK.
- Dukan, F., Ludvigsen, M., and Sørensen, A.J. (2011). Dynamic positioning system for a small size ROV with experimental results. In *IEEE OCEANS 2011 – Spain*, 1–10.
- Esfandiari, F. and Khalil, H.K. (1992). Output feedback stabilization of fully linearizable systems. *International Journal of Control*, 56(5), 1007–1037.
- Fernandes, D.A., Dukan, F., and Sørensen, A.J. (2012). Reference model for high performance and low energy consumption motions. In *IFAC NGCUV 2012 – Portugal*, 217–222.
- Fernandes, D.A., Sørensen, A.J., and Donha, D.C. (2013). Trajectory tracking motion control system for observation class ROVs. In *IFAC CAMS 2013 – Japan*, 251–256.
- Fossen, T.I. (2011). *Handbook of marine craft hydrodynamics and motion control*. John Wiley & Sons, Ltd., Chichester, UK.
- Franklin, G.F., Powell, J.D., and Emami-Naeini, A. (2009). *Feedback control of dynamic systems*. Prentice Hall, Inc., Upper Saddle River, 6th edition.
- Friedland, B. (1986). *Control system design: an introduction to state-space methods*. McGraw-Hill, Inc., New York.
- Hsu, L., Costa, R.R., Lizarralde, F., and da Cunha, J.P.V.S. (2000). Dynamic positioning system for remotely operated underwater vehicles. *IEEE Robotics and Automation Magazine*, 7(3), 21–31.
- Khalil, H.K. (2002). *Nonlinear systems*. Prentice Hall, Inc., Upper Saddle River, 3rd edition.
- Lewandowski, E.M. (2004). *The dynamics of marine craft: maneuvering and seakeeping*, volume 22 of *Advanced Series on Ocean Engineering*. World Scientific Pub., Arlington.
- Ludvigsen, M., Sortland, B., Johnsen, G., and Singh, H. (2007). Applications of geo-referenced underwater photomosaics in marine biology and archaeology. *Oceanography*, 20(4), 140–149.
- Marsh, L., Copley, J.T., Huvenne, V.A.I., Tyler, P.A., and the Isis ROV facility (2013). Getting the bigger picture: using prec. Remotely Operated Vehicle (ROV) videography to acquire high-definition mosaic images of newly discovered hydrothermal vents in the southern ocean. *Deep Sea Research Part II: Topical Studies in Oceanography*, 92(0), 124–135.
- Omerdic, E., Toal, D., Nolan, S., and Ahmad, H. (2012). ROV LATIS: next generation smart underwater vehicle. In G.N. Roberts and R. Sutton (eds.), *Further advances in unmanned marine vehicles (IEE Control Eng. Series – Vol. 77)*, chapter 2, 9–44. IEE – The Inst. of Electrical Eng., Stevenage, UK.
- Singh, H., Roman, C., Pizarro, O., Eustice, R., and Can, A. (2007). Towards high-resolution imaging from underwater vehicles. *The International Journal of Robotics Research*, 26(1), 55–74.
- Smallwood, D.A. and Whitcomb, L.L. (2004). Model-based dynamic positioning of underwater robotic vehicles: theory and experiment. *Journal of Oceanic Engineering*, 29(1), 169–186.
- SNAME (1950). The Society of Naval Architects and Marine Engineers. Nomenclature for treating the motion of a submerged body through a fluid. In *Technical and Research Bulletin*, 1–5.
- Sørensen, A.J. (2013). *Marine control systems: propulsion and motion control of ships and ocean structures*. Lecture notes. Marine Technology Centre, Trondheim, Norway, 3rd edition.
- Sørensen, A.J., Dukan, F., Ludvigsen, M., Fernandes, D.A., and Candeloro, M. (2012). Development of dynamic positioning and tracking system for the ROV Minerva. In G.N. Roberts and R. Sutton (eds.), *Further Advances in Unmanned Marine Vehicles (IEE Control Eng. Series – Vol. 77)*, chapter 6, 113–128. IEE – The Inst. of Electrical Engineers, Stevenage, UK.

## Appendix A. NTNU'S ROV MINERVA

Minerva is a SUB-fighter 7500 ROV made by Sperre AS in 2003 for NTNU. The NTNU's Research Vessel (R/V) Gunnerus (<http://www.ntnu.edu/marine/gunnerus>) is the support vessel used to carry out operations with Minerva. The ROV is powered from, and communicates with, Gunnerus via a 600 m-long umbilical cable. It has five thrusters with fixed pitch propellers. The starboard and port thrusters are oriented 10° towards the longitudinal axis of Minerva. The lateral thruster has one propeller at each end of its shaft, whilst all the others have a single propeller each. A high-precision hydroacoustic positioning system HiPAP 500 by Kongsberg determines the position of Minerva relative to Gunnerus. The MCS is implemented on a cRIO, and programmed via LabVIEW, both by National Instruments. Further details can be found in Sørensen et al. (2012) and Dukan et al. (2011), for instance.